How to cite: *Angew. Chem. Int. Ed.* **2023,** *62,* e202218094
International Edition: doi.org/10.1002/anie.202218094
German Edition: doi.org/10.1002/ange.202218094

Glasses

Fabrication of Super-Sized Metal Inorganic-Organic Hybrid Glass with Supramolecular Network via Crystallization-Suppressing Approach

Mohamed A. Ali[+],[*] *Wessel M. W. Winters, Moushira A. Mohamed*[+], *Dezhi Tan, Guojun Zheng, Rasmus S. K. Madsen, Oxana V. Magdysyuk, Maria Diaz-Lopez, Biao Cai, Nan Gong, Yijue Xu, Ivan Hung, Zhehong Gan, Sabyasachi Sen, Hong-Tao Sun, Thomas D. Bennett, Xiaofeng Liu,*[*] *Yuanzheng Yue,*[*] *and Jianrong Qiu*[*]

Abstract: Metal coordination compound (MCC) glasses [e.g., metal-organic framework (MOF) glass, coordination polymer glass, and metal inorganic-organic complex (MIOC) glass] are emerging members of the hybrid glass family. So far, a limited number of crystalline MCCs can be converted into glasses by melt-quenching. Here, we report a universal wet-chemistry method, by which the super-sized supramolecular MIOC glasses can be synthesized from non-meltable MOFs. Alcohol and acid were used as agents to inhibit crystallization. The MIOC glasses demonstrate unique features including high transparency, shaping capability, and anisotropic network. Directional photoluminescence with a large polarization ratio (≈47 %) was observed from samples doped with organic dyes. This crystallization-suppressing approach enables fabrication of super-sized MCC glasses, which cannot be achieved by conventional vitrification methods, and thus allows for exploring new MCC glasses possessing photonic functionalities.

Introduction

Metal coordination compound (MCC) glasses are the fourth known family of melt-quenched glasses, besides the other inorganic, organic and metallic families.[1,2] They possess a network structure, in which metal nodes are coordinated to organic moieties. This new family of glass is considered to be a promising material for various applications, e.g., gas separation, energy storage and photonics.[3–15] Crystalline metal–organic framework (MOF), coordination polymer (CP), and metal inorganic-organic complex (MIOC), a subclass of MCC, are built up with three-dimensional (3D), two-dimensional (2D), one-dimensional (1D), or zero-dimensional (0D) network structure.[16–19] Several MOFs, CPs and MIOCs can be melted and quenched to bulk glasses, such that the MCC network is preserved after vitrification.[20–31] Ionic liquids were recently shown to facilitate the melting process of non-meltable MOF structures.[22] In the process of making MCC glasses (e.g., MOFs and CPs) using melting-quenching or hot-press techniques, which typically need high temperatures and/or pressure, the sizes of glass samples are limited to few

---

[*] M. A. Ali,[+] M. A. Mohamed,[+] G. Zheng, N. Gong, J. Qiu
State Key Laboratory of Modern Optical Instrumentation, College of Optical Science and Engineering, Zhejiang University
Hangzhou 310027 (China)
E-mail: mohamedali@zju.edu.cn
qjr@zju.edu.cn

W. M. W. Winters, R. S. K. Madsen, Y. Yue
Department of Chemistry and Bioscience, Aalborg University
9220 Aalborg (Denmark)
E-mail: yy@bio.aau.dk

D. Tan
Zhejiang Lab
Hangzhou 310027 (China)

O. V. Magdysyuk, M. Diaz-Lopez
Diamond Light Source, Harwell Science and Innovation Campus
Didcot, Oxfordshire OX11 0QX (UK)

B. Cai
School of Metallurgy and Materials, University of Birmingham
Birmingham, B15 2TT (UK)

Y. Xu, I. Hung, Z. Gan
National High Magnetic Field Laboratory
1800 E. Paul Dirac Drive, Tallahassee, FL-32310 (USA)

S. Sen
Department of Materials Science and Engineering, University of California at Davis
Davis, CA-95616 (USA)

H.-T. Sun
International Center for Materials Nanoarchitectonics (MANA), National Institute for Materials Science (NIMS)
1-2-1 Sengen, Tsukuba, Ibaraki 305-0047 (Japan)

T. D. Bennett
Department of Materials Science and Metallurgy, University of Cambridge
Cambridge CB30FS (UK)

X. Liu
School of Materials Science and Engineering, Zhejiang University
Hangzhou 310027 (China)
E-mail: xfliu@zju.edu.cn

[+] These authors contributed equally to this work.

millimeters.[5,10,12] In addition, the melting process at elevated temperatures has to be performed in an inert gas or vacuum, to protect the organic linkers from being decomposed during melting.[23,29] However, it was reported that the 2D CPs lose their structural periodicity after glass formation as the occurrence of a high degree of distortion around metal ions during melting.[28,29] Similar to MOFs and CPs, MIOCs suffer from sublimation during melting,[32,33] while few examples of MIOCs could be transformed into glasses by melting-quenching when the decomposition of organic moieties during melting at high temperatures was minimized.[2,13,30] Furthermore, amorphous MCCs can be obtained by mechanical milling methods.[1,20,28] Generally, the fabrication of bulk MCC glasses is difficult and hence restricts the practical applications of MCCs. To date, the fabrication of large-sized MCC glasses at low temperatures and under ambient conditions remains challenging.[34] Therefore, the development of an efficient and facile synthetic approach that enables the fabrication of large-sized MCC glasses with various structures and functionalities, is of utmost importance.

Here, we demonstrate a synthetic approach to prepare large-sized MCC glass in air and at low temperature (i.e., <373 K). Using this approach, we synthesize a novel hydrogen-bonded MIOC glass (i.e., $Zn(NO_3)_2(Hbim)_2$, Hbim = protonated benzimidazole)[35] through suppressing the crystallization of non-meltable 2D zeolitic-imidazolate framework-7-III (ZIF-7-III)[24] (i.e., $Zn_2(bim)_4$, bim = benzimidazole; ZIFs are a sub-set of MOFs[36]) in a solution, rather than the commonly used direct melt-quenching of MCCs.[2] It is expected that molecules including ethanol and nitric acid insert into the ZIF network, coordinate with the metal centers, and distort the framework by interrupting its structural periodicity, thereby transforming the framework into a hydrogen-bonded MIOC network. The addition of alcohol and acid induces significant geometric deformation of the ZIF, and finally results in a new MIOC glass with a supramolecular network. Accordingly, we performed systematic investigations into the composition, local structure, thermodynamics, and optical properties of the as-synthesized differences between the ZIF-7-III crystal and MIOC glass. Furthermore, using the crystallization-suppressing strategy on the zinc and cobalt-based ZIF-7-III crystals, we successfully fabricated large-sized MIOC glasses (i.e., $M(NO_3)_2(Hbim)_2$, M = Zn and Co). The as-synthesized glasses can be shaped as 3D bulk objects, fibers, and thick films, and show the capability to incorporate luminescent organic dyes into the glass network, and hence, display efficient and directional luminescence.

Results and Discussion

In the preparation of the ZIF-7-III crystal and MIOC glass samples (Figure 1a and Figure S1), we first dissolved $Zn(NO_3)_2.6H_2O$ and Hbim into 20 ml ethanol at room temperature (RT) with a molar ratio of Zn:Hbim = 1:2. The dissolution of $Zn(NO_3)_2.6H_2O$ and Hbim into ethanol led to the nucleation and formation of fragments of 2D ZIF-7-III network consisting of Zn and Hbim. When this solution was transferred into a capped Teflon jar and heated in an oven at 373 K for 1 day, crystalline ZIF-7-III was precipitated, as a result of the increase of both temperature and pressure inside the Teflon jar as well as the retaining of solvent amount during the heating process. ZIF-7-III possesses a supramolecular 2D layered structure (Figure 1b), which was created by self-assembly via CH-π stacking interaction between the monolayers.[24] In order to suppress the crystallization of the 2D framework of the ZIF-7-III and then to form 3D hydrogen-bonded MIOC glass network, the prepared solution was heated at 373 K for 1 h in air (i.e., @ atmospheric pressure). Consequently, a transparent glassy sample (labeled as undried MIOC glass) was obtained from the supramolecular MIOC that was connected with ethanol through H-bonding (Figure 1c).[37] Owing to the pressure drop inside the jar as well as the evaporation of ethanol during heating at 373 K in air, the crystallization of 2D ZIF-7-III fragments was suppressed by nitrate molecules, resulting in the hydrogen-bonded MIOC network with high geometrical deformation. In this network, Zn is coordinated tetrahedrally to two NO_3 and two Hbim, and the $Zn(NO_3)_2(Hbim)_2$ molecules are connected to each other through H-bonding (i.e., N–H···O).[35] However, the prolonged drying of the undried MIOC glass at 323 K for 1 month led to the evaporation of excess solvent and hence the formation of transparent bulk glass (labeled as MIOC glass). It is interesting to note that the large-sized MIOC glass can be synthesized by casting the glass into a silicone mold with a rectangular shape and then cooling it at 273 K to maintain its structural rigidity. Furthermore, the drying of the undried MIOC glass at 373 K for 1 day caused the brown color of the glass (labeled as brown MIOC glass). The powder X-ray diffraction (PXRD) measurements (Figure 1d) verified that the synthesized crystalline powder was isostructural to a previously synthesized ZIF-7-III crystal.[38,39] Meanwhile, the PXRD patterns of the undried MIOC, MIOC, and brown MIOC glasses (Figure 1d and Figure S2) confirmed that the structure of the as-synthesized glasses was highly disordered, since the Bragg peaks were all absent, and instead, two overlapped broad humps were observed. Surprisingly, the as-synthesized MIOC glass/ZIF-7-III crystal could be easily crystallized/vitrified to ZIF-7-III crystal/MIOC glass, respectively, through controlling the bonding between Zn and bim/Hbim/NO_3 (Figure S3a). Furthermore, the as-synthesized MIOC glass fully crystallized to ZIF-7-III crystals after immersing the glassy sample in water.[40] This is because water plays an important role in the removal of nitrate molecules that are coordinated to Zn atoms in the MIOC network. The elimination of nitrate content allows Zn atoms to coordinate to Hbim and consequently the network changes from MIOC (i.e., Hbim-Zn-NO_3) to ZIF-7-III crystal (i.e., Zn-bim-Zn). The crystallization of MIOC glass to ZIF-7-III crystal using water was confirmed by PXRD and scanning electron microscopy (SEM) measurements (Figures S3b and S3c). Furthermore, the conversion of ZIF-7-III crystal into MIOC glass can be realized using ethanol/HNO_3 solution as evidenced by PXRD measurements (Figure S3d). These results imply that water and ethanol/HNO_3

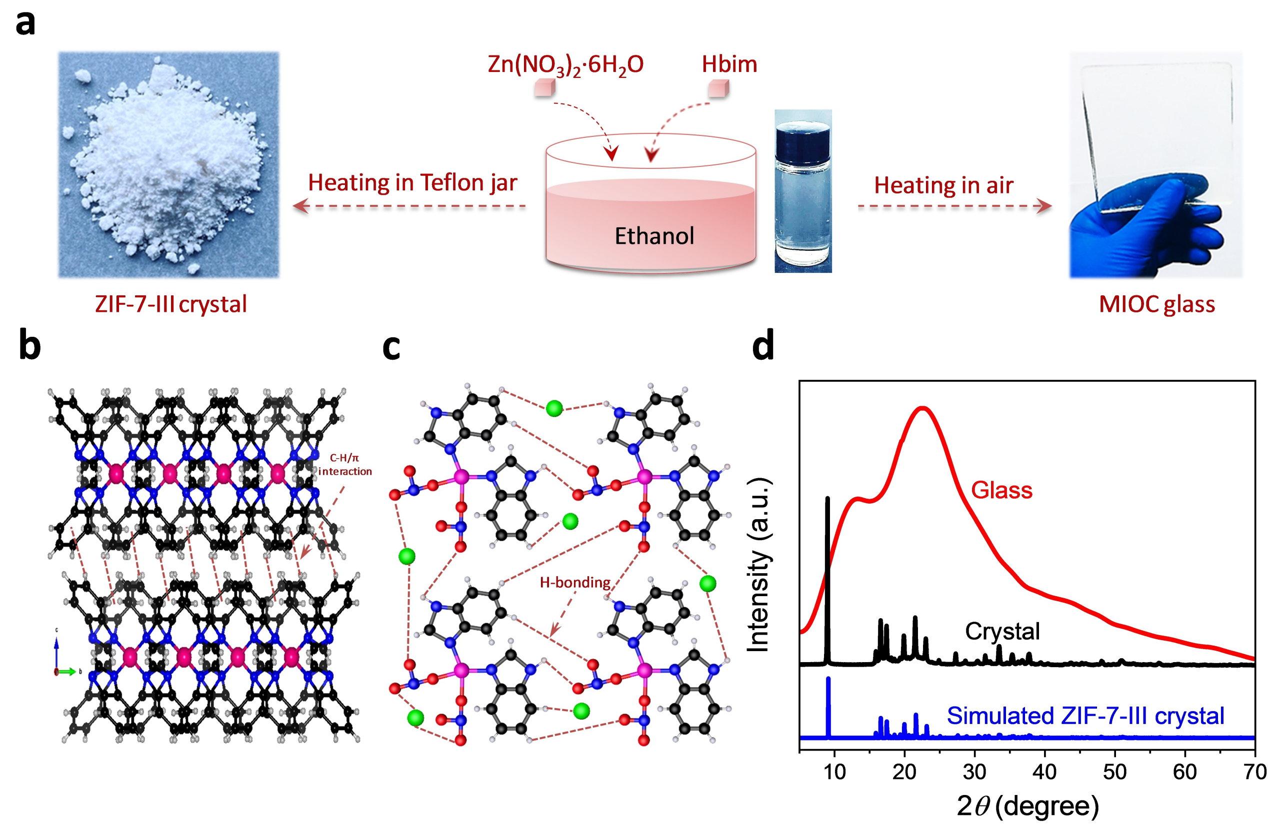

Figure 1. Synthesis of the ZIF-7-III crystal and MIOC glass. a, Schematic illustration for the preparation of the ZIF-7-III crystal and MIOC glass. The photograph of a) MIOC glass piece in the shape of rectangular with a dimension of 20 cm × 20 cm × 1 cm, was captured at 273 K. b) The architecture of the ZIF-7-III crystal, which illustrates layered structure along *c* axis and connected by CH-π interaction. c) The anticipated H-bonding between the hydrogen bonded MIOC network and ethanol in the glass sample. Red sphere, O; pink, Zn; black, C; blue, N; gray, H. and green, ethanol. d) PXRD patterns of the ZIF-7-III crystal and MIOC glass. The simulated pattern of the ZIF-7-III crystal is based on the single-crystal data (CCDC-675375).

solutions are necessary to devitrify MIOC glass and to suppress the crystallization of ZIF-7-III network, respectively. Moreover, we synthesized zinc and cobalt-based MIOC glasses with different solvents (Figures S4 and S5), implying that the crystallization-suppressing strategy of MOF is a versatile method for the fabrication of MIOC glasses. The as-synthesized zinc-based MIOC glasses exhibit high transparency in the visible and near-infrared (NIR) ranges even under an optical microscope (Figures S6 and S7).

The compositions of the as-synthesized ZIF-7-III crystals and MIOC glasses were investigated by several techniques, such as thermogravimetric analysis (TGA), inductively coupled plasma mass spectrometry (ICP-MS), CHNO analyzer, and solution ^{1}H nuclear magnetic resonance (NMR) measurements. The TGA traces of the crystalline and glassy samples (Figures S8) illustrate that the ZIF-7-III crystals do not undergo any weight loss prior to the decomposition at 973 K. The conversion of ZIF-7-III crystal into MIOC glass leads to the weakening of the network as a result of the interruption of the Zn-bim-Zn bonds.[25] Consequently, the degree of the thermal decomposition of the MIOC glass is much lower than that of ZIF-7-III crystal. The undried MIOC and MIOC glasses start to decompose at $T_{d1} = 373$ K by releasing the ethanol, and then the hydrogen-bonded MIOC decomposes at $T_{d2} = 473$ K. Furthermore, the brown MIOC glass samples directly decompose at 473 K, implying the evaporation of ethanol during drying at 373 K. Based on the observed weight loss in the TGA traces, the weight percentage (wt %) of the MIOC network and ethanol was measured and consequently the composition of the as-synthesized MIOC glass samples was calculated as shown in Table S1. The compositions of the as-synthesized ZIF-7-III crystals and MIOC glasses were further confirmed by ICP-MS and CHNO measurements as summarized in the Table S2.

Interestingly, the measured weight fraction of Zn, C, H, N, and O in the as-synthesized ZIF-7-III crystal and MIOC glasses are in line with the calculated values.[23] According to the elemental analysis results, we infer that the undried MIOC glass contains 88 wt % MIOC network and 12 wt % ethanol. After drying the wet glassy sample, the ethanol content decreases further to 3.5 wt % in the MIOC glass, and the brown MIOC glass is ethanol-free. The decrease of ethanol content in the glass samples after drying was confirmed by NMR measurement (Figure S9). The solution

^{1}H NMR measurements of the as-synthesized ZIF-7-III crystals and MIOC samples (Figure S10) reveal the decomposition of Hbim into protonated imidazole (Him) in the brown MIOC glasses, which is due to the presence of oxygen (e.g., in nitrates) in the glass network. The oxygen serves as an oxidizing agent and hence facilitates the decomposition of Hbim during drying.[41,42] These results explain the brown coloration of the MIOC glasses after drying at 373 K for 1 day. The measured Him/(Hbim+Him) values and the detailed compositions of the crystal and glass samples are given in Table 1.

Table 1: The nominal and the measured molar ratios of Him/(Hbim+Him) for the ZIF-7-III crystal, undried MIOC, MIOC, and brown MIOC glasses, including the detailed crystal/glass composition based on the TGA, ICP-MS, CHNO, and NMR measurements.

Sample	Measured Him/(Hbim+Him)	Composition (wt%)
ZIF-7-III crystal	0	$Zn_2(bim)_4$
Undried MIOC glass	0	88 $Zn(NO_3)_2(Hbim)_2$-12 Ethanol
MIOC glass	0	96.5 $Zn(NO_3)_2(Hbim)_2$-3.5 Ethanol
Brown MIOC glass	0.03	100 $Zn(NO_3)_2(Hbim)_{1.94}(Him)_{0.06}$

The isobaric heat capacity (C_p) curves of the undried MIOC (Figure S11a), MIOC (Figure 2a), and brown MIOC glasses (Figure S11b) show pronounced glass-transition temperatures (T_g) of 219 K ($\Delta C_p = 0.68\ J\,g^{-1}K^{-1}$), 255 K ($\Delta C_p = 0.57\ J\,g^{-1}K^{-1}$), and 281.3 K ($\Delta C_p = 0.5\ J\,g^{-1}K^{-1}$), respectively. The ΔC_p is inversely correlated with both the network connectivity and the number of the topological constraints.[43,44] These characteristics are rather low for molecular glasses (e.g., $\Delta C_p = 0.70\ J\,g^{-1}K^{-1}$ for $Zn(H_2PO_4)_2(1,2,4\text{-triazole})_2$ glass), and high for 3D glasses (e.g., $\Delta C_p = 0.16\ J\,g^{-1}K^{-1}$ for ZIF-4 glass and $\Delta C_p = 0.19\ J\,g^{-1}K^{-1}$ for ZIF-62 glass).[23,29,45] Accordingly, the observed high ΔC_p values for the as-synthesized MIOC glasses are likely attributed to their discrete molecular structure, while the increase of T_g value together with the decrease of its ΔC_p during the conversion of undried MIOC

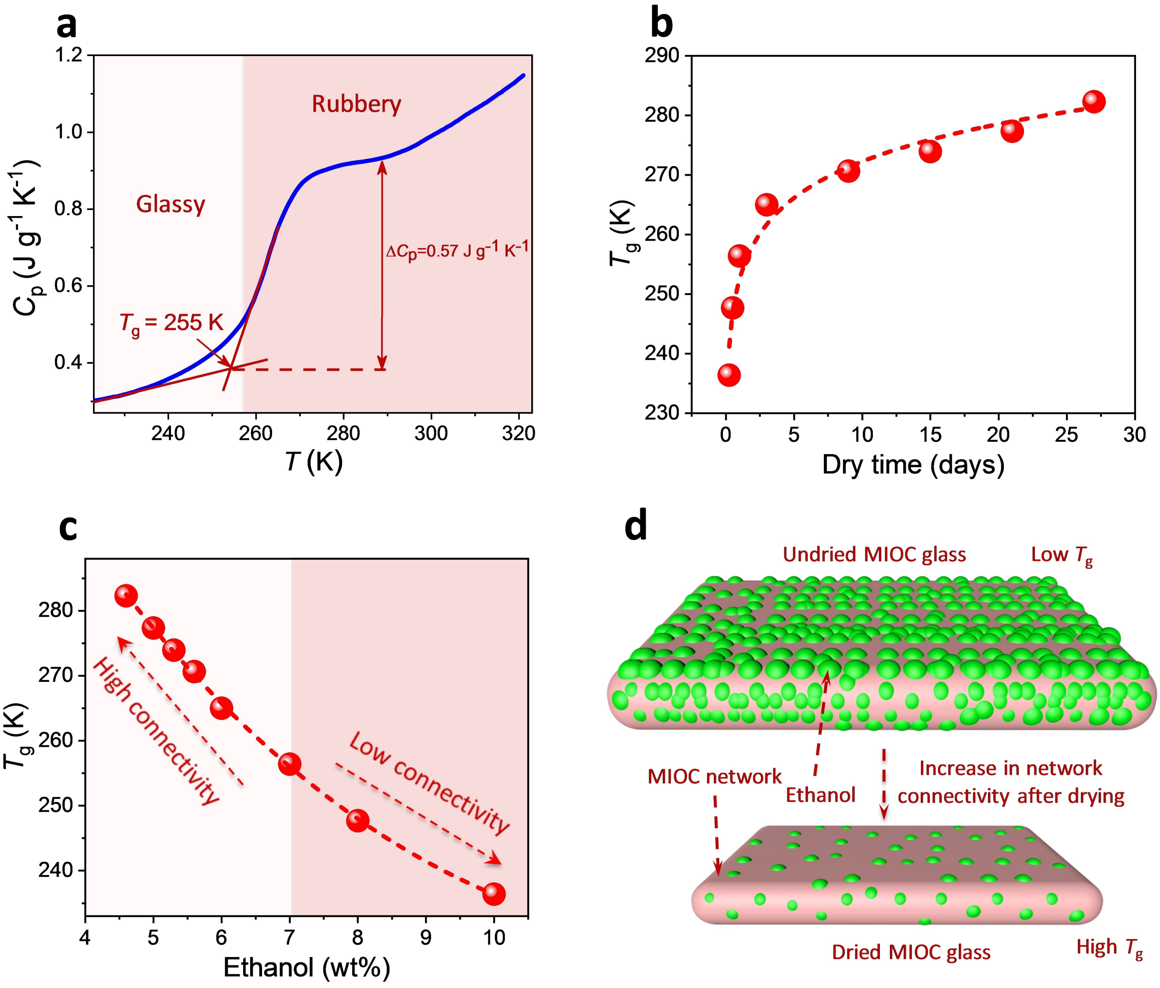

Figure 2. Glass transition of the MIOC glass. a) C_p trace of the MIOC glass. The T_g value of the MIOC glass as a function of, b) drying time at 343 K and c) ethanol content. d) Schematic illustration for the microstructural features of the MIOC network during drying process.

glass into MIOC glass and brown MIOC glasses could be explained by the increase of network connectivity. Based on the compositional and calorimetric analysis of the glass samples, it is evident that the T_g value of the glassy samples is sensitive to the ethanol content. We further measured the T_g values and the quantity of the solvent in the undried MIOC glass using differential scanning calorimetry (DSC) and TGA (Figure S12) for samples fabricated with different drying durations at 343 K. Thus we derived the dependence of T_g on the drying time (Figure 2b) and ethanol content (Figure 2c). In Figures 2b and 2c, it can be seen that T_g increases with increasing drying time and decreasing the ethanol content.[46] In addition, the ΔC_p value of the prepared glasses decreases after drying (Figure 2a, Figure S11). These trends suggest that the gradual removal of ethanol from the hydrogen-bonded Hbim-Zn-NO_3 network leads to an increase of the network connectivity as well as the strengthening of the interaction between MIOC molecules (Figure 2d). Furthermore, the T_g value of ethanol or water, even in nano-confinement, is significantly lower than that shown in Figure 2a.[47–50] Meanwhile, the ethanol-free glass sample (i.e. brown MIOC glass) exhibits an obvious T_g at 281.3 K. Therefore, the glass transition peak indeed originates from the glass transition of the hydrogen-bonded MIOC network. The occurrence of the glass transition in MIOC glasses suggests that these glasses exhibit the dynamic and thermodynamic behaviors of melt-quenched glasses. This suggests that the MIOC glass forms via a combined approach of sol-gel route and slow quenching.

To gain insights into the morphology of the as-synthesized samples, SEM imaging was performed on the 2D ZIF-7-III crystal and hydrogen-bonded MIOC glasses as shown in Figures S13 and S14. The SEM images of the ZIF-7-III crystals demonstrate ordered layers that stacked along *c* axis (Figure S13a), however, these layered structures disappear in the SEM images of the MIOC glasses and brown MIOC glasses (Figures S13b and S13c) as a result of the formation of the 3D supramolecular network. The elemental distribution mapping of the MIOC glass (Figure S14) confirm the enrichment of the glass network by Zn, C, N, and O. To examine the local structure of the crystalline and glassy samples, we measured the extended X-ray absorption fine structure (EXAFS) spectra at the Zn *K*-edge for the synthesized ZIF-7-III crystal and MIOC glasses (Figure 3a and Figure S15). The Fourier transforms of Zn *K*-edge EXAFS spectra for ZIF-7-III crystal and MIOC glasses are similar and exhibit one strong peak at 1.5 Å (this distance is not phase corrected, and is typically ca. 0.5 Å smaller than the actual distance), which was assigned to the Zn–N bond.[23] The fitting results of the EXAFS spectra (Figure S16 and Table S3) show that the Zn–N bond length is about 2 Å for the ZIF-7-III crystal and MIOC glasses. Due to the high similarity between Zn–N and Zn–O bond lengths in the tetrahedral configuration, we could not precisely calculate the Zn–O bond length for the glassy samples, where the Zn–O distance is comparable to the Zn–N distance (i.e., Zn–N=Zn–O $\approx$ 2 Å) in the zinc nitrate imidazole complex.[35] To further investigate and compare the local structure of the crystalline and glassy samples, X-ray total scattering experiments were conducted on the MIOC glass and ZIF-7-III crystal. The pair distribution function (PDF) D(*r*) data of the MIOC glass and ZIF-7-III crystal (Figure 3b) suggest that the correlations between Zn and Hbim remain intact in the MIOC glass, since the observed C–N, Zn–N, and Zn–C correlations in the glass sample are similar to those in ZIF-7-III crystal. Unlike ZIF-7-III crystal, the PDF data of the MIOC glass shows slight shifts in the correlations of C–N and Zn–N, indicating the contributions from N–O and O–O/Zn–O correlations, respectively. The increase in the intensities of the correlation peaks at 3.7 Å and 5 Å suggests a contribution from Zn-nitrate correlations. The Zn–Zn correlation was interrupted by nitrates, and hence, the medium-range order correlations (i.e., $r > 6$ Å) were not observed in the PDF curve of the glass sample. This indicates the conversion of ZIF-7-III network (i.e., Zn-bim-Zn) into MIOC (i.e., Hbim-Zn-NO_3). The molecular and electronic structure differences between ZIF-7-III crystal and MIOC glass were examined by NMR and X-ray photoelectron spectroscopy (XPS) measurements (Figures S17–S19 and Supporting Texts I–II). The ^{67}Zn magic-angle-spinning NMR (MAS NMR) spectra of the 2D ZIF-7-III crystal and MIOC glass collected at the two different magnetic fields of 19.6 and 35.2 T were shown in Figure 3c and Figure S18a. The spectra of the ZIF-7-III crystal indicate the presence of more than one Zn local environment, consistent with the results of previous X-ray refinement studies,[38,39] indicating the presence of two distinct tetrahedral ZnN_4 environments. Therefore, these line shapes were simulated simultaneously with two sets of NMR parameters corresponding to the two Zn environments. Such simulations (Figures S18b and S18c) yield the isotropic chemical shift δ_{iso}, quadrupolar coupling constant C_Q and asymmetry parameter η of the electric field gradient tensor for these two environments: $\delta_{iso}=293.5$ and 294.4 ppm, $C_Q=9.2$ and 10.8 MHz, and $\eta=0$ and 0.3, respectively. It may be noted that these δ_{iso} values are characteristic of Zn atoms in tetrahedral ZnN_4 environments in various ZIFs, whereas the C_Q values are significantly higher than those in the typical range of 1–6 MHz, reported for the 3D ZIF crystal structure,[51,52] and hence is likely characteristic of low-dimensional ZIFs, such as ZIF-7-III, where the ZnN_4 tetrahedra form 2D layered structures. Unlike the crystal spectra, the ^{67}Zn MAS NMR spectra of the MIOC glass show a significantly broader peak for the higher field, indicating a rather large broadening contribution from the chemical shift distribution, implying a high degree of short-range disorder around ZnN_2O_2 as well from the presence of multiple sites of Zn with different degree of distortion.[51,52,35] The H-bonding in the networks of glassy MIOC samples was evaluated by Raman measurement (Figure S20 Table S4, and Supporting Text III).[53] As the T_g value of the as-synthesized MIOC glass is below 273 K, MIOC glass is dynamically flexible at RT and it can be drawn to a fiber using a tapered rod. To evaluate the anisotropic properties of the glass fiber, polarized micro-Raman spectra were recorded with the polarization of the excitation light parallel and perpendicular to the longitudinal axis of the MIOC fiber with a diameter of 200 µm

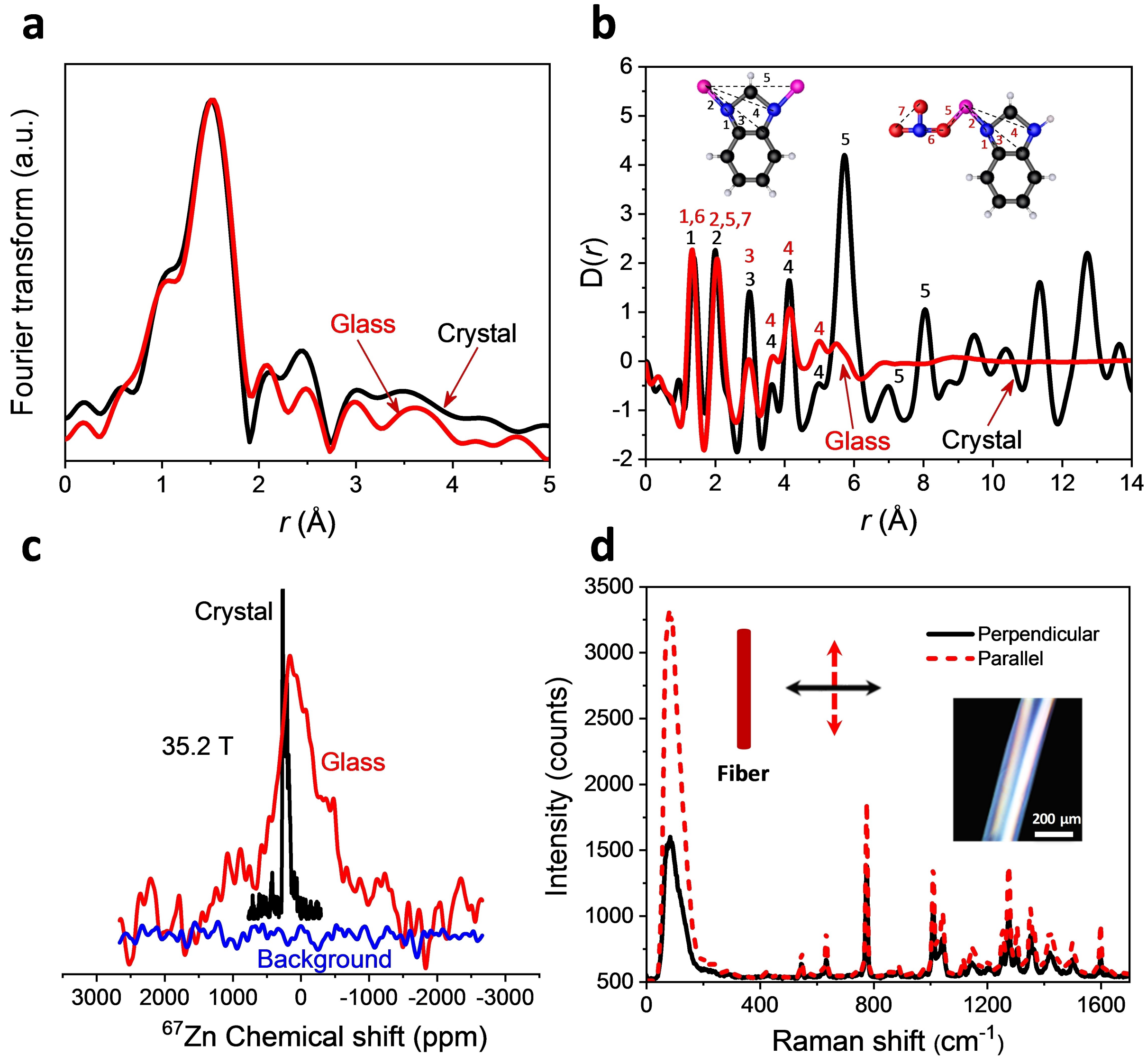

Figure 3. Structural investigations on the ZIF-7-III crystal and MIOC glass. a) Fourier transform of the Zn-K edge EXAFS spectra for the ZIF-7-III crystal and MIOC glass. b) X-ray PDF data of the ZIF-7-III crystal and MIOC glass with Hbim-Zn-NO_3 and Zn-bim geometries identifying peaks 1 to 7; Red sphere, O; pink, Zn; black, C; blue, N and gray, H. c) ^{67}Zn MAS NMR spectra of the ZIF-7-III crystal and MIOC glass recorded at magnetic field of 35.2 T. d) Polarized micro-Raman spectra recorded with the excitation light parallel and perpendicular to the longitudinal axis of the MIOC glass fiber with a diameter of 200 μm. The inset of d is the cross-polarized optical microscope image of the MIOC fiber.

(Figure 3d). The Raman spectra show that the Hbim resonance peaks are greater in intensity when the direction of excitation polarization is parallel to the fiber axis. Furthermore, there is no difference between the two polarized spectra of the bulk MIOC glass (Figure S21a). In addition, the intensities of the lattice vibration (@ 100 cm^{-1}) and the Hbim bending vibration (@ 775 cm^{-1}) peaks (Figure S21b) significantly increase by 1.66 and 1.3 times after changing the excitation polarization from perpendicular to parallel to the axis, indicating that the MIOC molecules were preferentially oriented along the axis.[54] Due to the orientation of the hydrogen-bonded MIOC along the fiber axis, birefringence was observed under the cross-polarized optical microscope (inset of Figure 3d). The alignment of the MIOC network along the fiber axis suggests that the as-drawn MIOC fiber possesses anisotropic local structure. The shrinkage of the undried MIOC glass fiber is discussed in Supporting Text IV (Figures S22 and S23 and Movie S1).

To explore the photonic application of the as-synthesized MIOC glass, we doped the undried MIOC (Figure S24) and MIOC glasses (Figures 4a and 4b) with luminescent dyes, such as coumarin 120 (C120), fluorescein (F), rhodamine 6G (R6G), and rhodamine B (RB). The optical properties of dye-doped undried MIOC and MIOC glasses were investigated by absorption, photoluminescence (PL), lifetime, and PL quantum yields (PLQY) spectroscopies (Figures S25–S28 and Supporting Text V). The PL spectra of the dye-doped undried MIOC and MIOC glasses

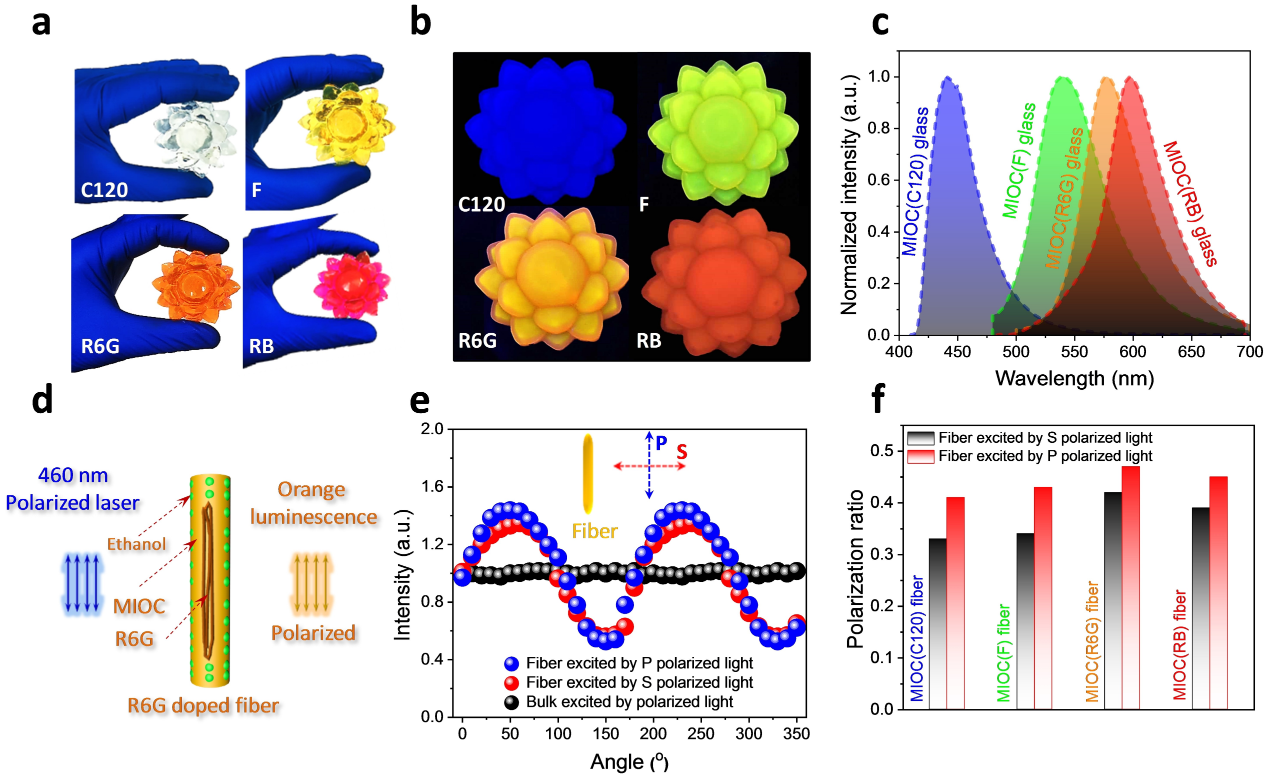

Figure 4. Luminescence performance of the MIOC glass doped with different types of dye molecules. Photographs of the MIOC glass doped with C120, F, R6G, and RB under a) natural light and b) UV-light irradiation (@ 365 nm). The MIOC glasses in (a) were prepared by casting the glass into a silicone mould with flower shape. The photograph of the MIOC glasses in the shape of flower, was captured at 273 K. c) PL spectra of the MIOC glass doped with C120 ($\lambda_{exc}=400$ nm), F ($\lambda_{exc}=470$ nm), R6G ($\lambda_{exc}=520$ nm), and RB ($\lambda_{exc}=520$ nm). d) Schematic illustration for the emitted light from the MIOC glass fiber doped with R6G. e) The variation of integrated PL intensity with different polarization angles for the MIOC glass fiber and MIOC bulk glass doped with R6G. P and S polarized light refer to the parallel and perpendicular polarization direction of the excitation light to the fiber axis, respectively. f) The polarization ratios of the MIOC fiber doped with C120, F, R6G, and RB under the excitation of polarized light. The MIOC(C120) and MIOC(F), MIOC(R6G), and MIOC(RB) fibers with a diameter of 200 μm were excited by 405 nm and 460 nm polarized lasers.

(Figure 4c and Figure S26) show efficient and sharp blue, green, orange, and red emissions.[55–58] The PLQY of the blue, green, orange, and red emissions (Figure S28) for the undried MIOC(C120), MIOC(F), MIOC(R6G), and MIOC(RB) glasses are 24 %, 62 %, 82 %, and 67 %, respectively. These values decrease to 17 %, 54 %, 36 %, and 42 % after drying owing to the increased coupling between dye molecules. According to previous studies,[59–63] layered structures loaded with dyes were widely used as polarized luminescence materials, however, their luminescence anisotropy is usually less than 0.15. Due to the anisotropic structure of the MIOC glass fiber as verified by polarized Raman spectroscopy, the dye molecules are expected to be molecularly oriented along the axial direction of 1D hydrogen bonded MIOC glass fiber, and thereby enhancing the ability of dyes to emit polarized light (Figure 4d). Thus, the dye-doped MIOC fibers with a diameter of 200 μm show strong polarized PL under the excitation of polarized light, while no polarized emission was observed in the bulk samples (Figure 4e and Figures S29 and S30). The excitation of the C120, F, R6G, and RB doped MIOC glass fibers (Figure 4f) by polarized laser perpendicular to the fiber axis (i.e., S polarized light) induces PL with polarization ratios (P_r) (defined as $(I_{max}-I_{min})/(I_{max}+I_{min})$, where I_{max} and I_{min} are the maximum and minimum intensities of the polarized emission) of 0.33, 0.34, 0.42, and 0.39, respectively. These values slightly increased to 0.41, 0.43, 0.47, and 0.45 for the fibers that were excited by polarized light parallel to the fiber axis (i.e., P polarized light). These results imply the high orientation of dye molecules along the fiber axis. Polarized PL was also observed in the dye-doped MIOC glass films with a thickness of 0.5 mm (Figure S31 and Supporting Text VI). The P_r values of the dye-doped MIOC glass films (i.e., $P_r=0.33$–0.35) are lower than that of the glass fiber (i.e., $P_r=0.41$–0.47), suggesting the less preferentially orientation of dye molecules in the MIOC thick films.

In a previous study, we found that 1D hydrogen-bonded ZnX_2Hbim_2-based MIOC crystals (X = Cl, Br, and I) can be vitrified by melt-quenching (@ 553 K) and the derived bulk and fiber glasses show the 362 K T_g.[30] In addition, the as-drawn $ZnCl_2Hbim_2$-based MIOC glass fiber possesses anisotropic structure.[13] After doping the $ZnCl_2Hbim_2$ glass fiber by C120, F, R6G, and RB dyes, directional PL with relatively low P_r values of 0.21–0.23, was observed from the fibers, while these P_r values decreased to 0.12–0.21 for the dye-doped $ZnCl_2Hbim_2$ glass films. By comparing the structural and optical properties of the $ZnCl_2Hbim_2$ and MIOC (i.e., 96.5 wt% $Zn(NO_3)_2Hbim_2$ + 3.5 wt% ethanol) glasses, we can infer that the Cl ion is replaced by NO_3 and a small amount of ethanol is incorporated into the MIOC glass network. The replacement of Cl by NO_3 together with the presence of ethanol in the glass network makes the nitrate-based MIOC network less rigid than the chloride-based MIOC network. This structural difference may explain why the nitrate-based MIOC glass is flexible during fiber drawing, resulting in the formation of MIOC glass fiber with higher structural anisotropy, as confirmed by the Raman measurement. The polarized Raman spectra of the $ZnCl_2Hbim_2$ glass fiber show that the intensity of the lattice vibration peak (@ 100 cm^{-1}) slightly increases by 1.12 after changing the excitation polarization from perpendicular to parallel direction to the fiber axis.[13] In comparison, the intensity of the lattice vibration peak increases to 1.66 for the nitrate-based MIOC glass fiber as shown in Figure 3d, implying the higher degree of local molecular orientation along the axis in glass fiber made from $Zn(NO_3)_2Hbim_2$ compared to $ZnCl_2Hbim_2$.[52] The increase in the structural anisotropy of the fiber enhances the polarizability of dye molecules and hence increases the P_r value of the emitted light.[63,64] This could explain why the dye-doped nitrate-based MIOC fiber exhibits the polarized light with P_r value (i.e., $P_r = 0.41$–0.47) that is twice the value of the chloride-based MIOC fiber (i.e., $P_r = 0.21$–0.23). These results also suggest that the MCC glasses prepared by the crystallization-suppressing approach be more promising for photonic applications compared to the melt-quenched glasses. It is interesting to note that the high polarization ratio of the as-synthesized nitrate-based MIOC fibers and thick films loaded with dyes is greater than those of perovskite nanocrystal embedded polymer composite films,[64,65] dye intercalated in ordered layered films,[59,60,63] dye-doped $ZnCl_2Hbim_2$ glass fibers and sheets[13] and oxide nanocrystal.[66]

Conclusions

A versatile wet-chemistry approach was established to fabricate hydrogen-bonded MIOC glasses, via the suppression of the crystallization of ZIFs. Accordingly, the crystallization of layered structures of the cobalt and zinc-based ZIF-7-III was prohibited in a mixture of alcohol and acid solutions, forming bulk glasses. The as-synthesized glass exhibited a glass transition peak, which was associated with the MIOC network. The super-sized MIOC glasses were fabricated, which possessed unique optical and structural properties. The dye-doped MIOC glass fibers and thick films exhibit directional PL as a result of their structural anisotropy. Our strategy provided a new route for the fabrication of MCC glasses, which could not be realized by conventional vitrification techniques. This work improved the understanding of the amorphization mechanisms of crystalline MCCs. In addition, the crystallization-suppressing strategy enables the incorporation of luminescent materials (e.g., dyes) into MCC glasses, which may find practical applications, especially in photonics.[67–69]

Acknowledgements

The current work was funded by the National Key R&D Program of China (Grant No. 2020YFB1805900), the National Natural Science Foundation of China (Grant No. 52050410326, U20A20211, 62175210), Open Funds of State Key Laboratory of Precision Spectroscopy, East China Normal University, State Key Laboratory of High Field Laser Physics, Shanghai Institute of Optics and Fine Mechanics, Chinese Academy of Sciences and the Fundamental Research Funds for the Central Universities. T.D.B acknowledges the Royal Society for a University Research Fellowship (UF150021), the University of Canterbury Te-WhareWānanga o Waitaha, New Zealand, for a University of Cambridge Visiting Canterbury Fellowship, and the Leverhulme Trust for a Philip Leverhulme Prize (2019). Y.Y. acknowledges funding from Independent Research Fund Denmark under grant no. 1026-00318B. H.-T.S acknowledges the funding support from the JSPS KAKENHI (21H01743, 21K18942). A portion of this work was performed at the National High Magnetic Field Laboratory, which was supported by the National Science Foundation Cooperative Agreement No. DMR-1644779 and the State of Florida. We are grateful to the staff at the BL14W1 beamline at the Shanghai Synchrotron Radiation Facility for X-ray absorption measurement. Synchrotron diffraction and PDF measurements were performed on Beamline I15-1 (XPDF) at Diamond Light Source (beamtime cy30401-1). We acknowledge Søren Strandskov Sørensen for the help with PDF analysis.

Conflict of Interest

The authors declare no conflict of interest.

Data Availability Statement

Research data are not shared.

Keywords: Glassy Metal Coordination Compounds · Luminescent Glass · Polarized Light · Crystallization-Suppressing

---

[1] T. D. Bennett, S. Horike, *Nat. Rev. Mater.* **2018**, *3*, 431–440.
[2] M. A. Ali, X. Liu, J. Qiu, *J. Non-Cryst. Solids* **2022**, *597*, 121936.
[3] C. W. Gao, Z. J. Jiang, S. B. Qi, P. X. Wang, L. R. Jensen, M. Johansen, C. K. Christensen, Y. F. Zhang, D. B. Ravnsbæk, Y. Yue, *Adv. Mater.* **2022**, *34*, 2110048.
[4] Y. Wang, H. Jin, Q. Ma, K. Mo, H. Mao, A. Feldhoff, X. Cao, Y. Li, F. Pan, Z. Jiang, *Angew. Chem. Int. Ed.* **2020**, *59*, 4365–4369; *Angew. Chem.* **2020**, *132*, 4395–4399.

[5] L. Frentzel-Beyme, M. Kloß, P. Kolodzeiski, R. Pallach, S. Henke, *J. Am. Chem. Soc.* **2019**, *141*, 12362–12371.

[6] L. Frentzel-Beyme, M. Kloß, R. Pallach, S. Salamon, H. Moldenhauer, J. Landers, H. Wende, J. Debus, S. Henke, *J. Mater. Chem. A* **2019**, *7*, 985–990.

[7] J. Hou, P. Chen, A. Shukla, A. Krajnc, T. Wang, X. Li, R. Doasa, L. H. G. Tizei, B. Chan, D. N. Johnstone, R. Lin, T. U. Schülli, I. Martens, D. Appadoo, M. S. Ari, Z. Wang, T. Wei, S. Lo, M. Lu, S. Li, E. B. Namdas, G. Mali, A. K. Cheetham, S. M. Collins, V. Chen, L. Wang, T. D. Bennett, *Science* **2021**, *374*, 621–625.

[8] M. A. Ali, X. Liu, Y. Li, J. Ren, J. Qiu, *Inorg. Chem.* **2020**, *59*, 8380–8386.

[9] M. A. Ali, J. Ren, T. Zhao, X. Liu, Y. Hua, Y. Yue, J. Qiu, *ACS Omega* **2019**, *4*, 12081–12087.

[10] A. Qiao, H. Tao, M. Carson, S. Aldrich, L. Thirion, T. Bennett, J. Mauro, Y. Yue, *Opt. Lett.* **2019**, *44*, 1623–1625.

[11] S. Vaidya, O. Veselska, A. Zhadan, M. Diaz-Lopez, Y. Joly, P. Bordet, N. Guillou, C. Dujardin, G. Ledoux, F. Toche, R. Chiriac, A. Fateeva, S. Horike, A. Demessence, *Chem. Sci.* **2020**, *11*, 6815–6823.

[12] Z. Fan, C. Das, A. Demessence, R. Zheng, S. Tanabe, Y. S. Wei, S. Horike, *Chem. Sci.* **2022**, *13*, 3281–3287.

[13] M. A. Ali, X. Liu, H. T. Sun, J. Ren, J. Qiu, *Chem. Mater.* **2022**, *34*, 2476–2483.

[14] Y. Zhang, Y. Wang, H. Xia, P. Gao, Y. Cao, H. Jin, Y. Li, *Chem. Commun.* **2022**, *58*, 9548–9551.

[15] H. Xia, H. Jin, Y. Zhang, H. Song, J. Hu, Y. Huang, Y. Li, *J. Membr. Sci.* **2022**, *655*, 120611.

[16] R. Banerjee, A. Phan, B. Wang, C. Knobler, H. Furukawa, M. O'Keeffe, O. M. Yaghi, *Science* **2008**, *319*, 939–943.

[17] J. Yang, Y. B. Zhang, Q. Liu, C. A. Trickett, E. G. Puebla, M. A. Monge, H. Cong, A. Aldossary, H. Deng, O. M. Yaghi, *J. Am. Chem. Soc.* **2017**, *139*, 6448–6455.

[18] D. Umeyama, S. Horike, M. Inukai, T. Itakura, S. Kitagawa, *J. Am. Chem. Soc.* **2015**, *137*, 864–870.

[19] G. Li, D. Zhu, X. Wang, Z. Su, M. R. Bryce, *Chem. Soc. Rev.* **2020**, *49*, 765–838.

[20] M. F. Thorne, A. F. Sapnik, L. N. McHugh, A. M. Bumstead, C. C. Blas, D. S. Keeble, M. D. Lopez, P. A. Chater, D. A. Keen, T. D. Bennett, *Chem. Commun.* **2021**, *57*, 9272–9275.

[21] R. Gaillac, P. Pullumbi, K. A. Beyer, K. W. Chapman, D. A. Keen, T. D. Bennett, F. X. Coudert, *Nat. Mater.* **2017**, *16*, 1149–1154.

[22] V. Nozari, C. Calahoo, J. M. Tuffnell, D. A. Keen, T. D. Bennett, L. Wondraczek, *Nat. Commun.* **2021**, *12*, 5703.

[23] T. D. Bennett, Y. Yue, P. Li, A. Qiao, H. Tao, N. G. Greaves, T. Richards, G. I. Lampronti, S. A. T. Redfern, F. Blanc, O. K. Farha, J. T. Hupp, A. K. Cheetham, D. A. Keen, *J. Am. Chem. Soc.* **2016**, *138*, 3484–3492.

[24] Y. Peng, Y. Li, Y. Ban, H. Jin, W. Jiao, X. Liu, W. Yang, *Science* **2014**, *346*, 1356–1359.

[25] M. Liu, R. D. McGillicuddy, H. Vuong, S. Tao, A. H. Slavney, M. I. Gonzalez, S. J. L. Billinge, J. A. Mason, *J. Am. Chem. Soc.* **2021**, *143*, 2801–2811.

[26] S. S. Nagarkar, H. Kurasho, N. T. Duong, Y. Nishiyama, S. Kitagawa, S. Horike, *Chem. Commun.* **2019**, *55*, 5455–5458.

[27] C. Das, T. Ogawa, S. Horike, *Chem. Commun.* **2020**, *56*, 8980–8983.

[28] W. Chen, S. Horike, D. Umeyama, N. Ogiwara, T. Itakura, C. Tassel, Y. Goto, H. Kageyama, S. Kitagawa, *Angew. Chem. Int. Ed.* **2016**, *55*, 5195–5200; *Angew. Chem.* **2016**, *128*, 5281–5286.

[29] D. Umeyama, N. P. Funnell, M. J. Cliffe, J. A. Hill, A. L. Goodwin, Y. Hijikata, T. Itakura, T. Okubo, S. Horike, S. Kitagawa, *Chem. Commun.* **2015**, *51*, 12728–12731.

[30] M. A. Ali, X. Liu, B. Xu, Y. Li, M. A. Mohamed, Y. Yue, J. Qiu, *ACS Mater. Lett.* **2022**, *4*, 2613–2621.

[31] B. Zhou, Z. Qi, D. Yan, *Angew. Chem. Int. Ed.* **2022**, *61*, e202208735; *Angew. Chem.* **2022**, *134*, e202208735.

[32] M. Cölle, J. Gmeiner, W. Milius, H. Hillebrecht, W. Brütting, *Adv. Funct. Mater.* **2003**, *13*, 108–112.

[33] L. S. Sapochak, A. Padmaperuma, N. Washton, F. Endrino, G. T. Schmett, J. Marshall, D. Fogarty, P. E. Burrows, S. R. Forrest, *J. Am. Chem. Soc.* **2001**, *123*, 6300–6307.

[34] Z. Yin, Y. B. Zhang, H. B. Yu, M. H. Zeng, *Sci. Bull.* **2020**, *65*, 1432–1435.

[35] A. Sy, A. H. Barry, F. B. Amor, A. Driss, M. Gayea, A. S. Sall, *Acta Crystallogr. Sect. E* **2009**, *65*, m1238.

[36] K. S. Park, Z. Ni, A. P. Cote, J. Y. Choi, R. Huang, F. J. U. Romo, H. K. Chae, M. O. Keeffe, O. M. Yaghi, *Proc. Natl. Acad. Sci. USA* **2006**, *103*, 10186–10191.

[37] J. Hou, A. F. Sapnik, T. D. Bennett, *Chem. Sci.* **2020**, *11*, 310–323.

[38] P. Zhao, G. I. Lampronti, G. O. Lloyd, M. T. Wharmby, S. Facq, A. K. Cheetham, S. A. T. Redfern, *Chem. Mater.* **2014**, *26*, 1767–1769.

[39] Q. F. Yang, X. B. Cui, J. H. Yu, J. Lu, X. Y. Yu, X. Zhang, J. Q. Xu, Q. Hou, T. G. Wang, *CrystEngComm* **2008**, *10*, 1534–1541.

[40] J. Yang, Q. Zhang, J. Y. Lee, H. P. Too, *J. Colloid Interface Sci.* **2007**, *308*, 157–161.

[41] H. Yin, H. Kim, J. Choi, A. C. K. Yip, *Chem. Eng. J.* **2015**, *278*, 293–300.

[42] J. B. James, Y. S. Lin, *J. Phys. Chem. C* **2016**, *120*, 14015–14026.

[43] M. M. Smedskjaer, J. C. Mauro, R. E. Youngman, C. L. Hogue, M. Potuzak, Y. Yue, *J. Phys. Chem. B* **2011**, *115*, 12930–12946.

[44] H. Liu, M. M. Smedskjaer, H. Tao, L. R. Jensen, X. Zhao, Y. Yue, *Phys. Chem. Chem. Phys.* **2016**, *18*, 10887–10895.

[45] A. Qiao, T. D. Bennett, H. Tao, A. Krajnc, G. Mali, C. M. Doherty, A. W. Thornton, J. C. Mauro, G. N. Greaves, Y. Yue, *Sci. Adv.* **2018**, *4*, eaao6827.

[46] Y. Zhao, S. Y. Lee, N. Becknell, O. M. Yaghi, C. A. Angell, *J. Am. Chem. Soc.* **2016**, *138*, 10818–10821.

[47] G. P. Johari, A. Hallbrucker, E. Mayer, *Nature* **1987**, *330*, 552–553.

[48] O. Haida, H. Suga, S. Seki, *J. Chem. Thermodyn.* **1977**, *9*, 1133–1148.

[49] R. Souda, *J. Phys. Chem. C* **2011**, *115*, 8136–8143.

[50] S. Sen, S. H. Risbud, M. H. Bartl, *Acc. Chem. Res.* **2020**, *53*, 2869–2878.

[51] R. S. K. Madsen, A. Qiao, J. Sen, I. Hung, K. Chen, Z. Gan, S. Sen, Y. Yue, *Science* **2020**, *367*, 1473–1476.

[52] A. Sutrisno, V. V. Terskikh, Q. Shi, Z. Song, J. Dong, S. Y. Ding, W. Wang, B. R. Provost, T. D. Daff, T. K. Woo, Y. Huang, *Chem. Eur. J.* **2012**, *18*, 12251–12259.

[53] Y. Ban, Z. Li, Y. Li, Y. Peng, H. Jin, W. Jiao, A. Guo, P. Wang, Q. Yang, C. Zhong, W. Yang, *Angew. Chem. Int. Ed.* **2015**, *54*, 15483–15487; *Angew. Chem.* **2015**, *127*, 15703–15707.

[54] S. Inaba, H. Hosono, S. Ito, *Nat. Mater.* **2015**, *14*, 312–317.

[55] D. Cao, Z. Liu, P. Verwilst, S. Koo, P. Jangjili, J. S. Kim, W. Lin, *Chem. Rev.* **2019**, *119*, 10403–10519.

[56] R. Boonsin, G. Chadeyron, J. P. Roblin, D. Boyer, R. Mahiou, *J. Mater. Chem. C* **2016**, *4*, 6562–6569.

[57] I. Moreno-Villoslada, M. Jofré, V. Miranda, R. González, T. Sotelo, S. Hess, B. L. Rivas, *J. Phys. Chem. B* **2006**, *110*, 11809–11812.

[58] M. Acar, E. Bozkurt, K. Meral, M. Arık, Y. Onganer, *J. Lumin.* **2015**, *157*, 10–15.

[59] D. Yan, J. Lu, M. Wei, D. G. Evans, X. Duan, *J. Phys. Chem. B* **2009**, *113*, 1381–1388.

[60] D. Yan, J. Lu, J. Ma, M. Wei, S. Qin, L. Chen, D. G. Evans, X. Duan, *J. Mater. Chem.* **2010**, *20*, 5016–5024.

[61] W. Shi, Z. Sun, M. Wei, D. G. Evans, X. Duan, *J. Phys. Chem. C* **2010**, *114*, 21070–21076.
[62] T. Shi, Y. Lu, *Polymer* **2020**, *189*, 122167.
[63] F. López Arbeloa, V. M. Martínez, T. Arbeloa, I. L. Arbeloa, *J. Photochem. Photobiol. C* **2007**, *8*, 85–108.
[64] W. G. Lu, X. G. Wu, S. Huang, L. Wang, Q. Zhou, B. Zou, H. Zhong, Y. Wang, *Adv. Opt. Mater.* **2017**, *5*, 1700594.
[65] S. N. Raja, Y. Bekenstein, M. A. Koc, S. Fischer, D. Zhang, L. Lin, R. O. Ritchie, P. Yang, A. P. Alivisatos, *ACS Appl. Mater. Interfaces* **2016**, *8*, 35523–35533.
[66] E. Chaudan, J. Kim, S. T. Nenez, P. Goldner, O. L. Malta, J. Peretti, T. Gacoin, *J. Am. Chem. Soc.* **2018**, *140*, 9512–9517.
[67] X. Yang, D. Yan, *Chem. Sci.* **2016**, *7*, 4519–4526.
[68] D. Yan, Y. Tang, H. Lin, D. Wang, *Sci. Rep.* **2014**, *4*, 4337.
[69] R. Gao, M. S. Kodaimati, D. Yan, *Chem. Soc. Rev.* **2021**, *50*, 5564–5589.

Manuscript received: December 8, 2022
Accepted manuscript online: February 6, 2023
Version of record online: February 21, 2023